International Forum on Aeroelasticity and Structural Dynamics
IFASD 2026
17-21 June 2026, Goettingen, Germany

DIRECTLY-PHYSICAL SUBSPACE IDENTIFICATION FOR STRUCTURE-PRESERVING AEROSERVOELASTIC MODEL UPDATING

Özge Süelözgen[1], Keith Soal[2], Felix Stalla[3], Thiemo Kier[3], Gertjan Looye[3]

[1]German Aerospace Center (DLR), Institute of Aeroelasticity
Münchener Straße 20, 82234 Weßling, Germany
oezge.sueeloezgen@dlr.de

[2]German Aerospace Center (DLR), Institute of Aeroelasticity
Bunsenstraße 10, 37073 Göttingen, Germany

[3]German Aerospace Center (DLR), Institute of Aeroelasticity
Münchener Straße 20, 82234 Weßling, Germany

Keywords: Directly-physical subspace identification, Markov parameters, aeroelasticity, model updating

Abstract: This paper presents a directly-physical subspace identification approach for structure-preserving aeroservoelastic model updating. The proposed method combines a physics-based continuous-time aeroservoelastic model with data-driven Markov-parameter information obtained from subspace identification. Instead of replacing the nominal model by a black-box identified realization, the method updates physically meaningful parameters of the nominal continuous-time model. For each candidate parameter vector, the structured continuous-time model is assembled, discretized, and compared with Markov parameters extracted from an experimentally identified discrete-time model. An optional time-domain fitting term may be added to improve transient response correlation. The method is applied to a flexible wind-tunnel aeroservoelastic model with control-surface inputs and acceleration outputs. The updated model preserves the physical partition into elastic modal states, actuator states, aerodynamic lag states, control-surface lag states, and output-delay states.

1 INTRODUCTION

Reliable aeroservoelastic models are essential for flutter analysis, gust-load prediction, control-law design, and experimental validation of flexible aircraft configurations. In wind-tunnel testing, however, nominal physics-based models often deviate from measured dynamics. These discrepancies may originate from uncertain modal frequencies and damping ratios, aerodynamic influence coefficients, actuator dynamics, sensor projections, output-delay dynamics, or measurement scaling. Consequently, model updating is required to improve agreement with experimental data while maintaining the interpretability of the model.

System identification methods can provide accurate input-output models directly from experimental data. In particular, subspace identification methods are attractive because they can deliver discrete-time state-space realizations and Markov parameters in a numerically robust way [1–3]. However, the resulting state-space matrices are typically expressed in arbitrary realization coordinates. Therefore, although a black-box identified model can reproduce the

measured input-output dynamics, its states and matrices generally do not preserve the physical partition of an aeroservoelastic model.

Classical physics-based model updating follows the opposite philosophy. The update is performed on physically interpretable quantities, such as modal frequencies, damping ratios, aerodynamic coefficients, actuator gains, or time constants. This preserves model structure but requires a sufficiently rich and well-conditioned parameterization. If the parameterization is too restrictive, the updated model cannot reproduce the measured dynamics; if it is too flexible, the physical meaning of the update may be lost.

The present work follows a directly-physical subspace identification strategy, referred to here as DPSI. The key idea is to use subspace identification only to define data-driven dynamic targets, while the optimization variables remain physical parameters of the continuous-time aeroservoelastic model. The primary target is the sequence of Markov parameters of the identified input-output system. Markov parameters are directly related to the impulse response of a discrete-time system and can be computed from a state-space realization without depending on the particular state basis. Therefore, they are well suited as realization-independent targets for updating a structured physical model.

The method is applied to a flexible wind-tunnel configuration with multiple control-surface inputs and acceleration outputs. The nominal model contains modal structural states, actuator states, aerodynamic lag states, control-surface-related lag states, and output-delay states. The proposed update preserves this structure by optimizing a low-dimensional vector of physical parameters and comparing the resulting discrete-time Markov parameters with those obtained from subspace identification.

2 NOMINAL AEROSERVOELASTIC MODEL

2.1 Aeroelastic equations of motion in time-domain

The nominal aeroelastic model is represented in modal coordinates. Let u_f, $\dot{u}_f$, and $\ddot{u}_f$ denote the modal displacement, velocity, and acceleration vectors. The equations of motion result in the following reduced-order (modal) dynamics in a matrix form as

$$\mathbf{M}_{ff}\ddot{u}_f + \mathbf{B}_{ff}\dot{u}_f + \mathbf{K}_{ff}u_f = F_{\text{aero}}, \tag{1}$$

where $\mathbf{M}_{ff}$, $\mathbf{B}_{ff}$, and $\mathbf{K}_{ff}$ are the modal mass, damping, and stiffness matrices and F_{aero} are generalized unsteady aerodynamic forces. For a classically damped modal model, the modal operators are expressed as

$$\mathbf{K}_{ff} = \mathbf{M}_{ff}\mathbf{\Omega}^2, \qquad \mathbf{B}_{ff} = \mathbf{M}_{ff}2\mathbf{\Xi}\mathbf{\Omega}, \tag{2}$$

where

$$\mathbf{\Omega} = \text{diag}(\omega_1, \ldots, \omega_{n_f}), \qquad \mathbf{\Xi} = \text{diag}(\zeta_1, \ldots, \zeta_{n_f}). \tag{3}$$

2.2 Generalized aerodynamic forces

The unsteady aerodynamic forces are computed in the frequency domain using the Doublet-Lattice Method (DLM). The DLM is a linear potential-flow panel method for oscillating lifting surfaces in subsonic flow. It discretizes the aerodynamic lifting surfaces into a lattice of panels and relates harmonic downwash boundary conditions to the corresponding unsteady pressure

distribution. The method is widely used in aeroelastic analysis because it provides generalized aerodynamic influence coefficient matrices over a set of reduced frequencies [4, 5].

For the present aeroservoelastic model, the generalized aerodynamic forces are written as

$$F_{\text{aero}}(ik) = q_\infty \left[\mathbf{Q}_{ff}(ik)u_f(ik) + \mathbf{Q}_{fx}(ik)u_x(ik)\right], \tag{4}$$

where $q_\infty = \frac{1}{2}\rho V_{\text{TAS}}^2$ is the dynamic pressure, u_f denotes the modal displacement vector, and u_x denotes the control-surface deflection vector. The matrices $\mathbf{Q}_{ff}(ik)$ and $\mathbf{Q}_{fx}(ik)$ are the generalized aerodynamic influence coefficient matrices obtained from the DLM. The matrix $\mathbf{Q}_{ff}(ik)$ maps modal structural motion to generalized aerodynamic forces, while $\mathbf{Q}_{fx}(ik)$ maps control-surface motion to generalized aerodynamic forces.

The reduced frequency is defined as

$$k = \frac{\omega c_{\text{ref}}}{2V_{\text{TAS}}}, \tag{5}$$

where c_{ref} is the reference chord length and V_{TAS} is the true airspeed. Since the DLM provides aerodynamic matrices only at discrete reduced frequencies, a rational function approximation is subsequently used to obtain a time-domain state-space realization of the unsteady aerodynamic forces [6, 7].

To obtain a time-domain state-space realization, the generalized aerodynamic matrices are approximated using Roger's rational function approximation [6, 7]. The structural-motion aerodynamic matrix is approximated as

$$\mathbf{Q}_{ff}(ik) \approx \mathbf{Q}_{0ff} + ik\mathbf{Q}_{1ff} + (ik)^2\mathbf{Q}_{2ff} + \sum_{j=1}^{n_p} \frac{ik}{ik + \beta_j}\mathbf{Q}_{ff,\ell j}, \tag{6}$$

and the control-surface aerodynamic matrix as

$$\mathbf{Q}_{fx}(ik) \approx \mathbf{Q}_{0fx} + ik\mathbf{Q}_{1fx} + \sum_{j=1}^{n_p} \frac{ik}{ik + \beta_{x,j}}\mathbf{Q}_{fx,\ell j}. \tag{7}$$

The matrices $\mathbf{Q}_{0ff}$, $\mathbf{Q}_{1ff}$, and $\mathbf{Q}_{2ff}$ describe displacement-, velocity-, and acceleration-related aerodynamic contributions, respectively. The matrices $\mathbf{Q}_{0fx}$ and $\mathbf{Q}_{1fx}$ describe control-surface deflection and rate contributions. The remaining rational terms are represented by aerodynamic lag states.

2.3 Time-domain aeroservoelastic realization

The aerodynamic contribution associated with structural motion is written in time domain as

$$F_{\text{aero},f} = q_\infty \left[\mathbf{Q}_{0ff}u_f + \frac{c_{\text{ref}}}{2V_{\text{TAS}}}\mathbf{Q}_{1ff}\dot{u}_f + \left(\frac{c_{\text{ref}}}{2V_{\text{TAS}}}\right)^2 \mathbf{Q}_{2ff}\ddot{u}_f + \mathbf{Q}_{\text{lag}}x_{\text{lag}}\right]. \tag{8}$$

The aerodynamic contribution associated with control-surface motion is

$$F_{\text{aero},x} = q_\infty \left[\mathbf{Q}_{0fx}x_{\text{act}} + \frac{c_{\text{ref}}}{2V_{\text{TAS}}}\mathbf{Q}_{1fx}\dot{x}_{\text{act}} + \mathbf{Q}_{\text{lag},x}x_{\text{lag},x}\right]. \tag{9}$$

The actuator dynamics are represented by first-order systems:

$$\dot{x}_{\text{act}} = \mathbf{A}_{\text{act}} x_{\text{act}} + \mathbf{B}_{\text{act}} u_{\text{cmd}}. \tag{10}$$

For diagonal actuator channels,

$$\mathbf{A}_{\text{act}} = \operatorname{diag}\left(-\frac{1}{\tau_1}, \ldots, -\frac{1}{\tau_{n_x}}\right), \qquad \mathbf{B}_{\text{act}} = \operatorname{diag}\left(\frac{K_1}{\tau_1}, \ldots, \frac{K_{n_x}}{\tau_{n_x}}\right). \tag{11}$$

Substituting (10) into (9) yields

$$F_{\text{aero},x} = q_\infty \Bigg[\mathbf{Q}_{0fx} x_{\text{act}} + \frac{c_{\text{ref}}}{2V_{\text{TAS}}} \mathbf{Q}_{1fx} \left(\mathbf{A}_{\text{act}} x_{\text{act}} + \mathbf{B}_{\text{act}} u_{\text{cmd}} \right) + \mathbf{Q}_{\text{lag},x} x_{\text{lag},x} \Bigg]. \tag{12}$$

After moving the acceleration-related aerodynamic term to the left-hand side, the effective modal equation becomes

$$\mathbf{M}_{\text{eff}} \ddot{u}_f + \mathbf{B}_{\text{eff}} \dot{u}_f + \mathbf{K}_{\text{eff}} u_f = F_{\text{lag}} + F_{\text{act}}, \tag{13}$$

with

$$\mathbf{M}_{\text{eff}} = \mathbf{M}_{ff} - q_\infty \left(\frac{c_{\text{ref}}}{2V_{\text{TAS}}} \right)^2 \mathbf{Q}_{2ff}, \tag{14}$$

$$\mathbf{B}_{\text{eff}} = \mathbf{B}_{ff} - q_\infty \frac{c_{\text{ref}}}{2V_{\text{TAS}}} \mathbf{Q}_{1ff}, \tag{15}$$

and

$$\mathbf{K}_{\text{eff}} = \mathbf{K}_{ff} - q_\infty \mathbf{Q}_{0ff}. \tag{16}$$

The right-hand-side terms are

$$F_{\text{lag}} = q_\infty \mathbf{Q}_{\text{lag}} x_{\text{lag}} + q_\infty \mathbf{Q}_{\text{lag},x} x_{\text{lag},x}, \tag{17}$$

$$F_{\text{act}} = q_\infty \mathbf{Q}_{0fx} x_{\text{act}} + q_\infty \frac{c_{\text{ref}}}{2V_{\text{TAS}}} \mathbf{Q}_{1fx} \left(\mathbf{A}_{\text{act}} x_{\text{act}} + \mathbf{B}_{\text{act}} u_{\text{cmd}} \right). \tag{18}$$

2.4 Aerodynamic lag-state equations

The rational approximation of the unsteady aerodynamic forces introduces two sets of aerodynamic lag states. The first set is associated with structural modal motion and satisfies

$$\dot{x}_{\text{lag}} = \frac{V_{\text{TAS}}}{c_{\text{ref}}/2} \mathbf{R} x_{\text{lag}} + \mathbf{E}_f \dot{u}_f. \tag{19}$$

The second set is associated with control-surface motion and satisfies

$$\dot{x}_{\text{lag},x} = \frac{V_{\text{TAS}}}{c_{\text{ref}}/2} \mathbf{R}_x x_{\text{lag},x} + \mathbf{E}_x \left(\mathbf{A}_{\text{act}} x_{\text{act}} + \mathbf{B}_{\text{act}} u_{\text{cmd}} \right). \tag{20}$$

For n_p aerodynamic lag poles, the fixed coupling matrices are stacked identity matrices. For the structural lag states,

$$\mathbf{E}_f = \begin{bmatrix} \mathbf{I}_{n_f} \\ \mathbf{I}_{n_f} \\ \vdots \\ \mathbf{I}_{n_f} \end{bmatrix} \in \mathbb{R}^{n_p n_f \times n_f}, \tag{21}$$

and for the control-surface lag states,

$$\mathbf{E}_x = \begin{bmatrix} \mathbf{I}_{n_x} \\ \mathbf{I}_{n_x} \\ \vdots \\ \mathbf{I}_{n_x} \end{bmatrix} \in \mathbb{R}^{n_p n_x \times n_x}. \tag{22}$$

Here, n_f is the number of retained structural modes and n_x is the number of control-surface coordinates.

2.5 Sensor-acceleration output equation

The measured physical outputs are sensor accelerations. The modal accelerations are mapped to structural grid-point accelerations through the modal matrix $\mathbf{\Phi}_{gf}$, and then to sensor accelerations through the spline interpolation matrix $\mathbf{T}_{\text{spline}}$:

$$y_{\text{phys}} = \mathbf{T}_{\text{spline}} \mathbf{\Phi}_{gf} \ddot{u}_f. \tag{23}$$

The matrix $\mathbf{T}_{\text{spline}}$ is constructed using a classical beam-spline interpolation between structural finite-element nodes and sensor locations [8, 9]. Substituting the expression for $\ddot{u}_f$ into (23) gives the physical output equation

$$y_{\text{phys}} = \mathbf{C}_{\text{phys}} x_{\text{phys}} + \mathbf{D}_{\text{phys}} u_{\text{cmd}}. \tag{24}$$

2.6 Output-delay subsystem

The measurement-chain dynamics are represented by an output-delay subsystem. For output channel i, the delay subsystem is written as

$$\dot{x}_{\text{delay},i} = \mathbf{A}_{\text{delay},i} x_{\text{delay},i} + \mathbf{B}_{\text{delay},i} y_{\text{phys},i}, \qquad y_i = \mathbf{C}_{\text{delay},i} x_{\text{delay},i} + y_{\text{phys},i}. \tag{25}$$

The channel-wise realization is

$$\mathbf{A}_{\text{delay},i} = \begin{bmatrix} -A_{11,i} & -A_{12,i} \\ A_{21,i} & 0 \end{bmatrix}, \qquad \mathbf{B}_{\text{delay},i} = \begin{bmatrix} B_{11,i} \\ 0 \end{bmatrix}, \tag{26}$$

and

$$\mathbf{C}_{\text{delay},i} = \begin{bmatrix} -C_{11,i} & 0 \end{bmatrix}, \qquad D_{\text{delay},i} = 1. \tag{27}$$

Stacking all delay states yields

$$\dot{x}_{\text{delay}} = \mathbf{A}_{\text{delay}} x_{\text{delay}} + \mathbf{B}_{\text{delay}} y_{\text{phys}}, \qquad y = \mathbf{C}_{\text{delay}} x_{\text{delay}} + y_{\text{phys}}. \tag{28}$$

2.7 Complete continuous-time aeroservoelastic system

The physical aeroservoelastic state vector is defined as

$$x_{\text{phys}} = \begin{bmatrix} u_f \\ \dot{u}_f \\ x_{\text{act}} \\ x_{\text{lag}} \\ x_{\text{lag},x} \end{bmatrix}. \tag{29}$$

The physical subsystem is written as

$$\dot{x}_{\text{phys}} = \mathbf{A}_{\text{phys}} x_{\text{phys}} + \mathbf{B}_{\text{phys}} u_{\text{cmd}}, \qquad y_{\text{phys}} = \mathbf{C}_{\text{phys}} x_{\text{phys}} + \mathbf{D}_{\text{phys}} u_{\text{cmd}}. \tag{30}$$

Using the effective operators

$$\mathbf{M}_{\text{eff}} = \mathbf{M}_{ff} - q_\infty \left(\frac{c_{\text{ref}}}{2V_{\text{TAS}}} \right)^2 \mathbf{Q}_{2ff}, \tag{31}$$

$$\mathbf{B}_{\text{eff}} = \mathbf{B}_{ff} - q_\infty \frac{c_{\text{ref}}}{2V_{\text{TAS}}} \mathbf{Q}_{1ff}, \qquad \mathbf{K}_{\text{eff}} = \mathbf{K}_{ff} - q_\infty \mathbf{Q}_{0ff}, \tag{32}$$

the physical state matrix is

$$\mathbf{A}_{\text{phys}} = \begin{bmatrix} \mathbf{0} & \mathbf{I} & \mathbf{0} & \mathbf{0} & \mathbf{0} \\ \mathbf{A}_{21} & \mathbf{A}_{22} & \mathbf{A}_{23} & \mathbf{A}_{24} & \mathbf{A}_{25} \\ \mathbf{0} & \mathbf{0} & \mathbf{A}_{\text{act}} & \mathbf{0} & \mathbf{0} \\ \mathbf{0} & \mathbf{E}_f & \mathbf{0} & \dfrac{V_{\text{TAS}}}{c_{\text{ref}}/2}\mathbf{R} & \mathbf{0} \\ \mathbf{0} & \mathbf{0} & \mathbf{E}_x\mathbf{A}_{\text{act}} & \mathbf{0} & \dfrac{V_{\text{TAS}}}{c_{\text{ref}}/2}\mathbf{R}_x \end{bmatrix}. \tag{33}$$

The blocks in the structural acceleration row are

$$\mathbf{A}_{21} = -\mathbf{M}_{\text{eff}}^{-1}\mathbf{K}_{\text{eff}}, \tag{34}$$

$$\mathbf{A}_{22} = -\mathbf{M}_{\text{eff}}^{-1}\mathbf{B}_{\text{eff}}, \tag{35}$$

$$\mathbf{A}_{23} = \mathbf{M}_{\text{eff}}^{-1} q_\infty \left(\mathbf{Q}_{0fx} + \frac{c_{\text{ref}}}{2V_{\text{TAS}}} \mathbf{Q}_{1fx}\mathbf{A}_{\text{act}} \right), \tag{36}$$

$$\mathbf{A}_{24} = \mathbf{M}_{\text{eff}}^{-1} q_\infty \mathbf{Q}_{\text{lag}}, \tag{37}$$

$$\mathbf{A}_{25} = \mathbf{M}_{\text{eff}}^{-1} q_\infty \mathbf{Q}_{\text{lag},x}. \tag{38}$$

The physical input matrix is

$$\mathbf{B}_{\text{phys}} = \begin{bmatrix} \mathbf{0} \\ \mathbf{M}_{\text{eff}}^{-1} q_\infty \dfrac{c_{\text{ref}}}{2V_{\text{TAS}}} \mathbf{Q}_{1fx}\mathbf{B}_{\text{act}} \\ \mathbf{B}_{\text{act}} \\ \mathbf{0} \\ \mathbf{E}_x\mathbf{B}_{\text{act}} \end{bmatrix}. \tag{39}$$

The physical output matrix follows from the acceleration output equation. With

$$\mathbf{G}_s = \mathbf{T}_{\text{spline}} \mathbf{\Phi}_{gf}, \tag{40}$$

one obtains

$$\mathbf{C}_{\text{phys}} = \begin{bmatrix} \mathbf{C}_1 & \mathbf{C}_2 & \mathbf{C}_3 & \mathbf{C}_4 & \mathbf{C}_5 \end{bmatrix}, \tag{41}$$

where

$$\mathbf{C}_1 = -\mathbf{G}_s \mathbf{M}_{\text{eff}}^{-1} \mathbf{K}_{\text{eff}}, \tag{42}$$

$$\mathbf{C}_2 = -\mathbf{G}_s \mathbf{M}_{\text{eff}}^{-1} \mathbf{B}_{\text{eff}}, \tag{43}$$

$$\mathbf{C}_3 = \mathbf{G}_s \mathbf{M}_{\text{eff}}^{-1} q_\infty \left(\mathbf{Q}_{0fx} + \frac{c_{\text{ref}}}{2V_{\text{TAS}}} \mathbf{Q}_{1fx} \mathbf{A}_{\text{act}} \right), \tag{44}$$

$$\mathbf{C}_4 = \mathbf{G}_s \mathbf{M}_{\text{eff}}^{-1} q_\infty \mathbf{Q}_{\text{lag}}, \tag{45}$$

$$\mathbf{C}_5 = \mathbf{G}_s \mathbf{M}_{\text{eff}}^{-1} q_\infty \mathbf{Q}_{\text{lag},x}. \tag{46}$$

The corresponding direct input matrix is

$$\mathbf{D}_{\text{phys}} = \mathbf{G}_s \mathbf{M}_{\text{eff}}^{-1} q_\infty \frac{c_{\text{ref}}}{2V_{\text{TAS}}} \mathbf{Q}_{1fx} \mathbf{B}_{\text{act}}. \tag{47}$$

The full state vector is obtained by appending the output-delay states:

$$x = \begin{bmatrix} x_{\text{phys}} \\ x_{\text{delay}} \end{bmatrix}. \tag{48}$$

Substituting (30) into (28) gives the complete continuous-time aeroservoelastic model

$$\dot{x} = \mathbf{A}x + \mathbf{B}u_{\text{cmd}}, \qquad y = \mathbf{C}x + \mathbf{D}u_{\text{cmd}}, \tag{49}$$

with

$$\mathbf{A} = \begin{bmatrix} \mathbf{A}_{\text{phys}} & \mathbf{0} \\ \mathbf{B}_{\text{delay}} \mathbf{C}_{\text{phys}} & \mathbf{A}_{\text{delay}} \end{bmatrix}, \qquad \mathbf{B} = \begin{bmatrix} \mathbf{B}_{\text{phys}} \\ \mathbf{B}_{\text{delay}} \mathbf{D}_{\text{phys}} \end{bmatrix}, \tag{50}$$

and

$$\mathbf{C} = \begin{bmatrix} \mathbf{C}_{\text{phys}} & \mathbf{C}_{\text{delay}} \end{bmatrix}, \qquad \mathbf{D} = \mathbf{D}_{\text{phys}}. \tag{51}$$

3 DIRECTLY-PHYSICAL SUBSPACE IDENTIFICATION

3.1 Markov-parameter representation of the identified dynamics

The objective of the proposed DPSI method is to update the structured physical model using input-output information extracted from experimental data. Instead of comparing the matrices of a black-box identified realization directly with the physical model matrices, the comparison is performed using Markov parameters. This is essential because the state-space realization obtained from subspace identification is generally not unique. Any nonsingular similarity transformation produces an equivalent input-output model with different state matrices. Therefore, the identified state matrices themselves are not suitable as direct targets for physical model updating.

Consider a discrete-time state-space model

$$x_{k+1} = \mathbf{A}_d x_k + \mathbf{B}_d u_k, \qquad y_k = \mathbf{C}_d x_k + \mathbf{D}_d u_k. \tag{52}$$

The corresponding Markov parameters are the discrete-time pulse-response matrices

$$\mathbf{H}_0 = \mathbf{D}_d, \tag{53}$$

and

$$\mathbf{H}_k = \mathbf{C}_d \mathbf{A}_d^{k-1} \mathbf{B}_d, \qquad k = 1, 2, \ldots. \tag{54}$$

They describe the direct feedthrough and the subsequent impulse-response coefficients of the input-output system. Equivalently, they appear in the transfer-function expansion

$$\mathbf{G}_d(z) = \mathbf{D}_d + \mathbf{C}_d \left(z\mathbf{I} - \mathbf{A}_d\right)^{-1} \mathbf{B}_d = \sum_{k=0}^{\infty} \mathbf{H}_k z^{-k}. \tag{55}$$

The Markov sequence is invariant with respect to similarity transformations of the state vector. Hence, it provides a realization-independent input-output target. This property makes Markov parameters particularly attractive for combining subspace identification with a structured physical model. Markov parameters are closely related to impulse-response reconstruction and realization theory, including the Ho–Kalman realization framework and the eigensystem realization algorithm [10, 11]. In modern subspace identification, they can be obtained from the identified state-space realization or from the data equations used to estimate the extended observability and controllability matrices [1, 3].

Let the subspace-identified model $(\hat{\mathbf{A}}, \hat{\mathbf{B}}, \hat{\mathbf{C}}, \hat{\mathbf{D}})$ provide the target Markov sequence

$$\hat{\mathbf{H}}_0, \hat{\mathbf{H}}_1, \ldots, \hat{\mathbf{H}}_L. \tag{56}$$

For a given physical parameter vector θ, the structured continuous-time model is first assembled as

$$\left(\mathbf{A}(\theta), \mathbf{B}(\theta), \mathbf{C}(\theta), \mathbf{D}(\theta)\right). \tag{57}$$

It is then discretized using zero-order hold:

$$\left(\mathbf{A}_d(\theta), \mathbf{B}_d(\theta), \mathbf{C}_d(\theta), \mathbf{D}_d(\theta)\right) = \mathrm{c2d}\left(\mathbf{A}(\theta), \mathbf{B}(\theta), \mathbf{C}(\theta), \mathbf{D}(\theta), T_s\right). \tag{58}$$

The corresponding physical-model Markov parameters are

$$\mathbf{H}_0(\theta) = \mathbf{D}_d(\theta), \tag{59}$$

and

$$\mathbf{H}_k(\theta) = \mathbf{C}_d(\theta) \mathbf{A}_d(\theta)^{k-1} \mathbf{B}_d(\theta), \qquad k = 1, \ldots, L. \tag{60}$$

The Markov residual is defined as

$$\mathbf{E}_k^H(\theta) = \mathbf{W}_y \left[\hat{\mathbf{H}}_k - \mathbf{H}_k(\theta)\right] \mathbf{W}_u, \tag{61}$$

where $\mathbf{W}_y$ and $\mathbf{W}_u$ are output and input weighting matrices. The Markov-parameter objective is

$$J_H(\theta) = \sum_{k=0}^{L} w_k^2 \left\|\mathbf{E}_k^H(\theta)\right\|_F^2. \tag{62}$$

The scalar weights w_k may be used to emphasize specific portions of the impulse response. For example, early Markov parameters often carry robust information about the dominant input-output dynamics, whereas later Markov parameters may be more sensitive to noise, finite-data effects, and identification errors. A decreasing lag weighting can therefore be used to reduce the influence of uncertain long-lag terms.

The use of (62) is the central element of DPSI. The identified model provides the input-output impulse-response target, while the optimization variables remain physical parameters of the continuous-time aeroservoelastic model. Consequently, the final updated model remains structure-preserving and physically interpretable.

3.2 Optional time-domain fitting target

Although the Markov-parameter objective provides the main data-driven target, an additional time-domain fitting term can be included when direct transient-response agreement is desired. Let u_k^{exp} and y_k^{exp} denote the measured input and output sequences. Simulating the discretized structured model with the same input gives the model output $y_k(\theta)$. The time-domain residual is

$$e_k^t(\theta) = \mathbf{W}_t \left[y_k^{\mathrm{exp}} - y_k(\theta) \right], \tag{63}$$

where $\mathbf{W}_t$ is a time-domain output weighting matrix. The optional time-domain cost is

$$J_t(\theta) = \sum_{k=1}^{N} \left\| e_k^t(\theta) \right\|_2^2 . \tag{64}$$

This term is not required for the Markov-parameter-based update. It is introduced only as an optional supplement to improve selected time-domain correlations or to include additional validation signals in the optimization.

3.3 Regularization and stability constraint

To avoid nonphysical parameter changes, a regularization term is added:

$$J_{\mathrm{reg}}(\theta) = \lambda_{\mathrm{reg}} \left\| \theta - \theta_0 \right\|_2^2 , \tag{65}$$

where θ_0 denotes the nominal parameter vector. The regularization term penalizes large deviations from the nominal model and improves the conditioning of the nonlinear least-squares problem.

The stability of the updated discrete-time model is monitored using the spectral radius of the discrete state matrix:

$$\rho(\theta) = \max_i \left| \lambda_i \left(\mathbf{A}_d(\theta) \right) \right| . \tag{66}$$

A soft stability penalty is introduced as

$$J_{\mathrm{stab}}(\theta) = \lambda_{\mathrm{stab}} \max \left(\rho(\theta) - \rho_{\max}, 0 \right)^2 . \tag{67}$$

This term penalizes candidate models whose discrete-time poles approach or exceed the prescribed stability threshold $\rho_{\max}$.

3.4 DPSI optimization problem

The total objective function is written as

$$J(\theta) = J_H(\theta) + \mu_t J_t(\theta) + J_{\mathrm{reg}}(\theta) + J_{\mathrm{stab}}(\theta). \tag{68}$$

The scalar μ_t controls the optional time-domain contribution. Setting $\mu_t = 0$ results in a purely Markov-parameter-based DPSI update, whereas $\mu_t > 0$ includes time-domain fitting as an additional target.

The optimization problem is formulated as a nonlinear least-squares problem,

$$\theta^\star = \arg\min_\theta \left\| r(\theta) \right\|_2^2 , \tag{69}$$

where $r(\theta)$ is the stacked residual vector containing the weighted Markov residuals, optional time-domain residuals, regularization residuals, and stability residual. The updated continuous-time aeroservoelastic model is then obtained directly as

$$(\mathbf{A}^\star, \mathbf{B}^\star, \mathbf{C}^\star, \mathbf{D}^\star) = (\mathbf{A}(\theta^\star), \mathbf{B}(\theta^\star), \mathbf{C}(\theta^\star), \mathbf{D}(\theta^\star)) \,. \tag{70}$$

Thus, the final model is not obtained by applying a discrete-to-continuous transformation to an updated black-box realization. Instead, it is assembled directly from the optimized physical parameter vector.

3.5 Optimization parameters

The physical update vector is defined as

$$\theta = \begin{bmatrix} \alpha \\ \beta \\ \gamma_{Q0ff} \\ \gamma_{Q1ff} \\ \gamma_{Q2ff} \\ \gamma_{Q\mathrm{lag}} \\ \gamma_{Q\mathrm{lag},x} \\ \gamma_R \\ \gamma_{R_x} \\ \gamma_{Q0fx} \\ \gamma_{Q1fx} \\ \gamma_\tau \\ \gamma_K \end{bmatrix} . \tag{71}$$

The modal frequencies and damping ratios are updated by

$$\omega_i^{\mathrm{upd}} = \omega_i^{\mathrm{nom}}(1+\alpha_i), \qquad \zeta_i^{\mathrm{upd}} = \zeta_i^{\mathrm{nom}} + \beta_i. \tag{72}$$

The updated structural matrices are reconstructed as

$$\mathbf{K}_{ff}^{\mathrm{upd}} = \mathbf{M}_{ff}\left(\mathbf{\Omega}^{\mathrm{upd}}\right)^2, \qquad \mathbf{B}_{ff}^{\mathrm{upd}} = \mathbf{M}_{ff} 2\mathbf{\Xi}^{\mathrm{upd}}\mathbf{\Omega}^{\mathrm{upd}}. \tag{73}$$

The aerodynamic matrices are updated using low-dimensional scaling parameters. For $r \in \{0,1,2\}$,

$$\mathbf{Q}_{rff}^{\mathrm{upd}} = \mathbf{S}_r \mathbf{Q}_{rff}^{\mathrm{nom}} \mathbf{S}_r, \tag{74}$$

where $\mathbf{S}_r$ is a diagonal scaling matrix acting on selected modal coordinates. The lag-feedback matrices are updated by column-group scaling:

$$\mathbf{Q}_{\mathrm{lag}}^{\mathrm{upd}}(:, \mathcal{I}_g) = (1+\gamma_{Q\mathrm{lag},g})\mathbf{Q}_{\mathrm{lag}}^{\mathrm{nom}}(:, \mathcal{I}_g), \tag{75}$$

with an analogous expression for $\mathbf{Q}_{\mathrm{lag},x}$. The lag-pole matrices are updated as

$$\mathbf{R}^{\mathrm{upd}}(\mathcal{I}_g, \mathcal{I}_g) = (1+\gamma_{R,g})\mathbf{R}^{\mathrm{nom}}(\mathcal{I}_g, \mathcal{I}_g), \tag{76}$$

and similarly for $\mathbf{R}_x$.

The control-surface aerodynamic matrices are updated by actuator-column scaling:

$$\mathbf{Q}_{0fx}^{\mathrm{upd}} = \mathbf{Q}_{0fx}^{\mathrm{nom}} \mathrm{diag}(1+\gamma_{Q0fx}), \qquad \mathbf{Q}_{1fx}^{\mathrm{upd}} = \mathbf{Q}_{1fx}^{\mathrm{nom}} \mathrm{diag}(1+\gamma_{Q1fx}). \tag{77}$$

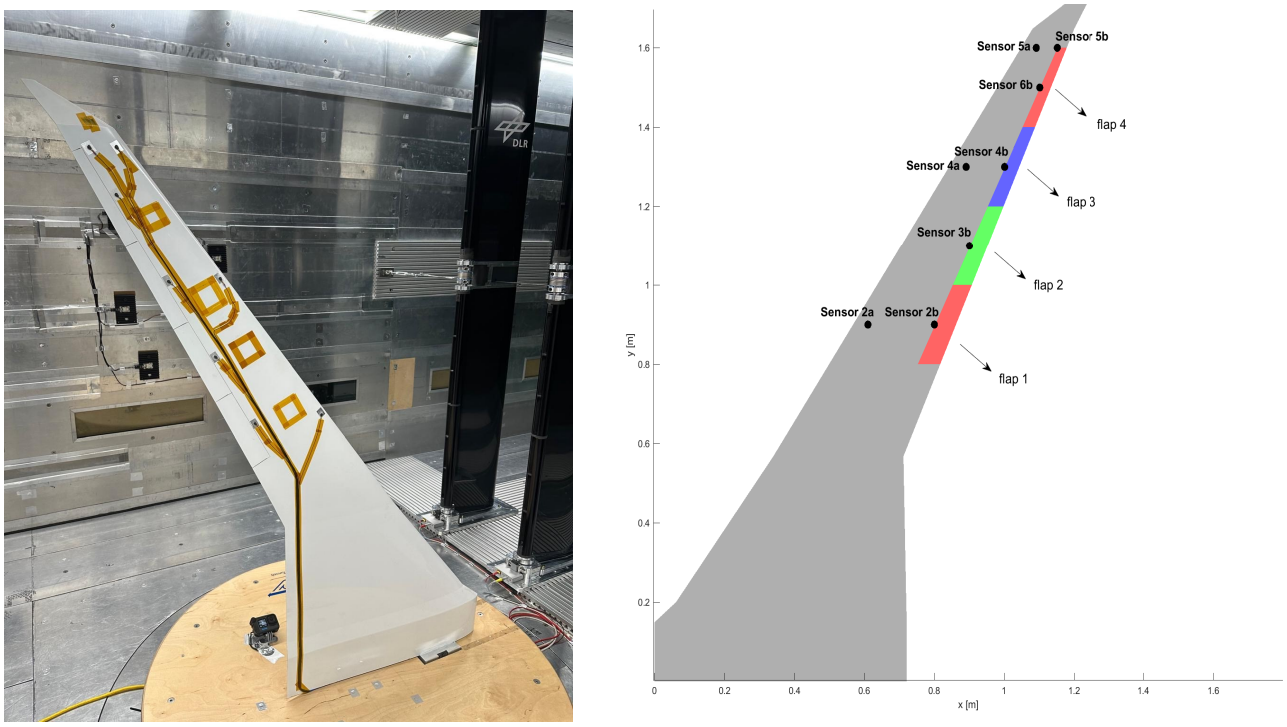
Finally, the actuator time constants and gains are updated according to

$$\tau_i^{\mathrm{upd}} = \tau_i^{\mathrm{nom}}(1+\gamma_{\tau,i}), \qquad K_i^{\mathrm{upd}} = K_i^{\mathrm{nom}}(1+\gamma_{K,i}). \tag{78}$$

This parameterization restricts the update to physically interpretable quantities and preserves the block structure of the aeroservoelastic model.

4 WIND-TUNNEL USE CASE

The proposed DPSI method is applied to a rigidly mounted flexible wind-tunnel aeroservoelastic model excited by four independently actuated trailing-edge flaps, located over the outboard part of the wing, using repeated chirp inputs at different freestream velocities of 30, 40 and 50 m/s, with eight vertical accelerometers as outputs. An overview of the wing planform along with its sensors' location is shown in Fig.1. The experimental data used in this research were acquired from the test campaigns conducted as part of the SAFER2 [12] project at the DNW-NWB, a low-speed wind tunnel of Göttinger type, situated at the DLR (German Aerospace Center) site in Braunschweig. The subspace-identified discrete-time model has been provided within the framework of operational modal analysis during wind-tunnel testing from the team of Department of Structural Dynamics and System Identification, Institute of Aeroelasticity, German Aerospace Center (DLR).



(a) Experimental setup for the aeroelastic wing demonstrator

(b) Sensor positions on the demonstrator

Figure 1: Aeroelastic wing demonstrator.

4.1 Data handling and target-model preparation

The experimental data considered in this work correspond to the operating condition at $V_{\mathrm{TAS}} = 50\ \mathrm{m/s}$. The aeroelastic wing demonstrator is excited via commanded control-surface deflections generating repeated logarithmic sweeps in the frequency range of $f_{\mathrm{exc}} \in [3, 15]$ Hz acting as inputs of the system, Fig.2, while eight sensors record vertical accelerations representing the outputs of the system, Fig.3.

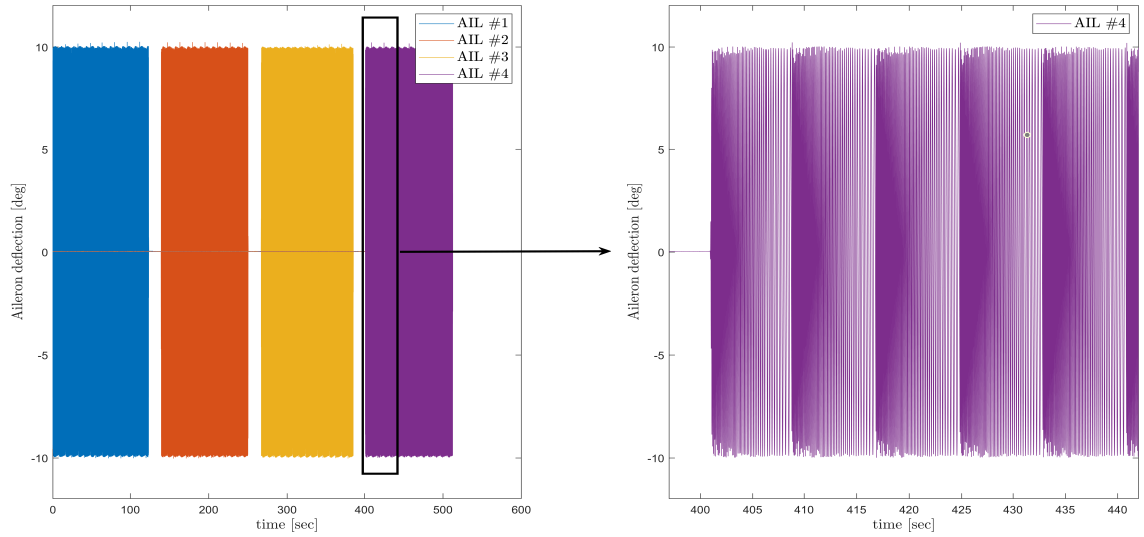


Figure 2: Flap deflections at $V_{\text{TAS}} = 50m/s$

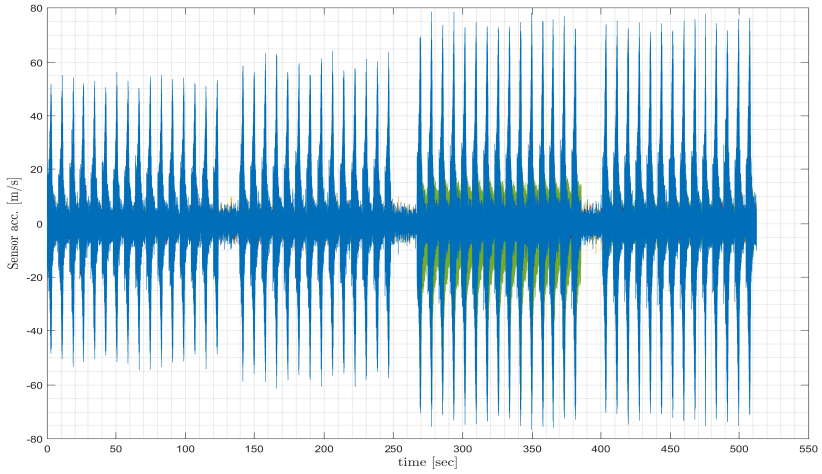


Figure 3: Measured vertical accelerations recorded by eight sensors

The sampling time is $T_s = 0.01$ s. The target input-output dynamics are provided by a subspace-identified discrete-time model. The identified realization has order $n_{\text{SSI}} = 40$. It is written as

$$x_{k+1}^{\text{SSI}} = \hat{\mathbf{A}}_d x_k^{\text{SSI}} + \hat{\mathbf{B}}_d u_k, \qquad y_k = \hat{\mathbf{C}}_d x_k^{\text{SSI}} + \hat{\mathbf{D}}_d u_k. \tag{79}$$

The SSI realization is used to compute the target Markov parameters,

$$\hat{\mathbf{H}}_0 = \hat{\mathbf{D}}_d, \tag{80}$$

$$\hat{\mathbf{H}}_k = \hat{\mathbf{C}}_d \hat{\mathbf{A}}_d^{k-1} \hat{\mathbf{B}}_d, \qquad k = 1, \ldots, L. \tag{81}$$

In the present work, the Markov horizon is selected as $L = 100$. With $T_s = 0.01$ s, this corresponds to a Markov time window of 1 s.

For the time-response fitting, and validation of the updated model the measurement record is divided into four sequential flap-actuation segments of shorter duration. Each segment consists of a pre-actuation interval of 1 s, a flap excitation interval of 24 s, and a post-actuation interval of 1 s, resulting in a segment duration of $T_{\mathrm{seg}} = 26$ s. Since the four flaps are deflected one after another, the total recording time is $T_{\mathrm{tot}} = 4T_{\mathrm{seg}} + 5\ \mathrm{s} = 101\ \mathrm{s}$. During each flap excitation, three logarithmic chirp cycles are generated. Therefore, the complete measurement data for validation contains a total of 12 logarithmic sweep cycles.

The theoretical aeroservoelastic model (Fig. 4) has a larger, physically partitioned state dimension than the SSI target model. The structural model contains $n_f = 15$ retained flexible modes, resulting in 15 modal displacement states and 15 modal velocity states. The actuator subsystem contains $n_x = 4$ actuator states. The rational-function approximation uses $n_p = 8$ aerodynamic lag poles. Therefore, the structural-motion lag subsystem has

$$n_{\mathrm{lag},f} = n_p n_f = 8 \cdot 15 = 120 \tag{82}$$

states, while the control-surface lag subsystem has

$$n_{\mathrm{lag},x} = n_p n_x = 8 \cdot 4 = 32 \tag{83}$$

states. Since the model has $n_y = 8$ measured outputs and each output channel is equipped with a second-order output-delay subsystem, the number of delay states is

$$n_{\mathrm{delay}} = 2n_y = 16. \tag{84}$$

The total state dimension of the structured continuous-time aeroservoelastic model is therefore

$$\begin{aligned} n_{\mathrm{ASE}} &= 2n_f + n_x + n_{\mathrm{lag},f} + n_{\mathrm{lag},x} + n_{\mathrm{delay}} \\ &= 2 \cdot 15 + 4 + 120 + 32 + 16 = 202. \end{aligned} \tag{85}$$

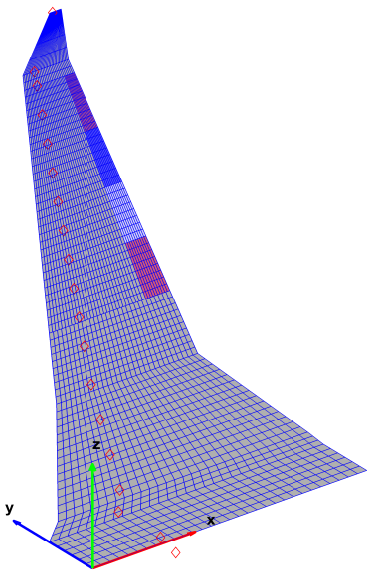


Figure 4: Aerodynamic panel model of the wing demonstrator with structural grids of the condensed FE model

Table 1 summarizes the main parameters of the SSI target model, the validation data, and the theoretical aeroservoelastic model.

Table 1: Overview of target model, validation data, and theoretical aeroservoelastic model parameters.

Quantity	Symbol	Value
True airspeed	V_{TAS}	$50\ \mathrm{m/s}$
Sampling time	T_s	$0.01\ \mathrm{s}$
SSI model order	n_{SSI}	40
Markov horizon	L	100
Time-domain weighting factor	μ_T	0.01
Validation excitation band	f_{exc}	3–15 Hz
Number of inputs	n_u	4
Number of measured outputs	n_y	8
Number of structural modes	n_f	15
Actuator states	n_x	4
RFA lag poles	n_p	8
Structural lag states	$n_{\mathrm{lag},f}$	120
Control-surface lag states	$n_{\mathrm{lag},x}$	32
Output-delay states	n_{delay}	16
Total theoretical model order	n_{ASE}	202

5 RESULTS

For the DPSI update, the first four aeroelastic modes were included in the physical parameterization. This choice was motivated by the modal content of the wind-on identified system and by the frequency range relevant for the considered operating condition. However, the active control-surface excitation was limited by the available actuator capacity. The commanded excitation covered the frequency range $f_{\mathrm{exc}} \in [3, 15]$ Hz, which was sufficient to excite mainly the first structural mode, located at approximately $8,4$ Hz.

Nevertheless, the first four aeroelastic modes could be identified from the wind-tunnel data due to the presence of aerodynamic excitation from the air stream and the resulting wind-on response of the flexible structure. Therefore, a distinction must be made between modes that are actively excited by the control-surface input and modes that are observable in the measured response under wind-on conditions. The first mode is both actively excited and clearly observable, whereas the higher modes are primarily identified through their contribution to the aeroelastic response induced by the flow field.

Consequently, the first four modes were retained in the DPSI update to preserve the relevant low-frequency aeroelastic modal subspace of the wind-on system. At the same time, the interpretation of the update results focuses primarily on the first mode, since it is the mode most strongly excited by the commanded input and therefore most directly constrained by the Markov-parameter and time-response targets. The updates of the higher modes are treated as secondary corrections that support the consistency of the overall aeroelastic model, but their quantitative interpretation is subject to the limited actuator capacity. In the following optimization results for the DPSI are discussed in detail.

5.1 Optimization results

The DPSI optimization converged after 51 iterations. The nominal Markov-parameter mismatch was reduced from $J_{H,\mathrm{nom}} = 7.0679 \times 10^5$ to $J_{H,\mathrm{upd}} = 3.5627 \times 10^5$. This corresponds to a reduction of the objective function by

$$\Delta J_H = -49.59\ \%. \tag{86}$$

Further the optimization reduced the total objective function (Eq. 68) by approximately $59,82\%$ relative to the nominal model. The results indicate a significant improvement of the input-output impulse-response representation of the structured aeroservoelastic model with respect to the subspace-identified Markov-parameter target. Figure 5 compares relative errors of Markov parameters between nominal and updated model vs.target SSI.

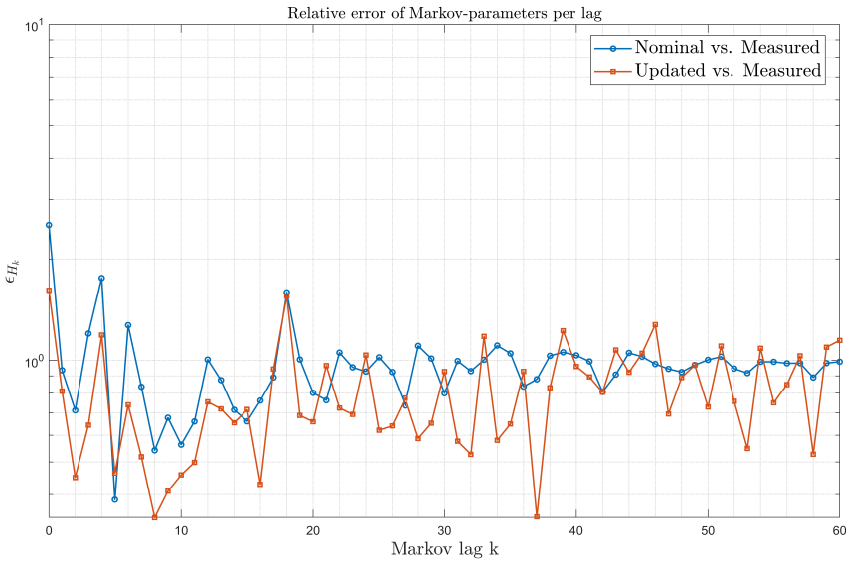


Figure 5: Relative error of Markov parameters per lag (nom. model vs. SSI and updated model vs. SSI)

The discrete-time spectral radius increased from $\rho(\mathbf{A}_{d,\mathrm{nom}}) = 0.952$ to $\rho(\mathbf{A}_{d,\mathrm{upd}}) = 0.989$. Although the updated model is closer to the stability boundary, it remains stable since

$$\rho(\mathbf{A}_{d,\mathrm{upd}}) < 1. \tag{87}$$

This behaviour is expected, since the optimization improves the dynamic agreement with the identified system while still being constrained by the stability penalty and physical parameter bounds.

The optimized parameter distribution shows that the largest corrections occur in the aerodynamic and actuator-related terms rather than in the modal frequency updates. This is physically plausible for the present wind-tunnel case, since the first structural mode is the dominant actively excited mode, while the remaining dynamics are influenced by aerodynamic lag effects, control-surface dynamics, and sensor/output-chain effects. The moderate changes in α_ω indicate that the nominal structural frequencies are largely retained, whereas the aerodynamic correction parameters modify the effective stiffness, damping, apparent mass, and lag contributions required to match the identified Markov sequence. The increase of the spectral radius after updating indicates that the updated system has moved closer to the identified dynamic behaviour,

but it remains stable. Overall, the results demonstrate that the DPSI update improves the input-output Markov representation while preserving the structured continuous-time aeroservoelastic model.

A summary of the main optimization results is given in Table 2. The optimized parameter values are listed in Tables 3–7.

Table 2: Summary of the DPSI optimization results.

Quantity	**Symbol**	**Value**
Number of iterations	–	51
Nominal Markov mismatch	$J_{H,\mathrm{nom}}$	7.0679×10^5
Updated Markov mismatch	$J_{H,\mathrm{upd}}$	3.5627×10^5
Markov objective-function change	ΔJ_{H}	$-49.59\ \%$
Total objective-function change	ΔJ	$-59.82\ \%$
Nominal spectral radius	$\rho(\mathbf{A}_{d,\mathrm{nom}})$	0.951679
Updated spectral radius	$\rho(\mathbf{A}_{d,\mathrm{upd}})$	0.988641

Table 3: Updated structural modal parameters.

Parameter	**Mode 1**	**Mode 2**	**Mode 3**	**Mode 4**
α_ω	0.01397	0.004715	0.003561	-0.06309
$\Delta\zeta$	0.0027155	0.0029474	-0.015277	0.01863

Table 4: Updated quasi-steady aerodynamic correction parameters.

Parameter	**Mode 1**	**Mode 2**	**Mode 3**	**Mode 4**
γ_{0f}	0.02930	0.40000	0.19738	0.15682
γ_{1f}	0.12817	0.02315	-0.15860	0.39009
γ_{2f}	-0.25670	0.19410	-0.37312	0.33060

Table 5: Updated aerodynamic lag-force correction parameters.

Parameter	**Pole 1**	**Pole 2**	**Pole 3**	**Pole 4**
$\gamma_{\ell f}$	-0.01036	0.01642	-0.00832	-0.00172
$\gamma_{\ell x}$	-0.02247	0.01036	0.00513	-0.03418
Parameter	**Pole 5**	**Pole 6**	**Pole 7**	**Pole 8**
$\gamma_{\ell f}$	0.00206	-0.00385	0.04385	-0.13670
$\gamma_{\ell x}$	0.00338	0.26746	-0.26775	0.34403

Table 6: Updated aerodynamic lag-pole correction parameters.

Parameter	**Pole 1**	**Pole 2**	**Pole 3**	**Pole 4**
$\gamma_{\beta f}$	-0.01371	-0.01786	0.00461	0.01586
$\gamma_{\beta x}$	-0.05850	0.00291	0.02137	-0.01264
Parameter	**Pole 5**	**Pole 6**	**Pole 7**	**Pole 8**
$\gamma_{\beta f}$	-0.01890	-0.03658	0.12645	0.01979
$\gamma_{\beta x}$	-0.02100	0.81417	-0.00304	-0.29856

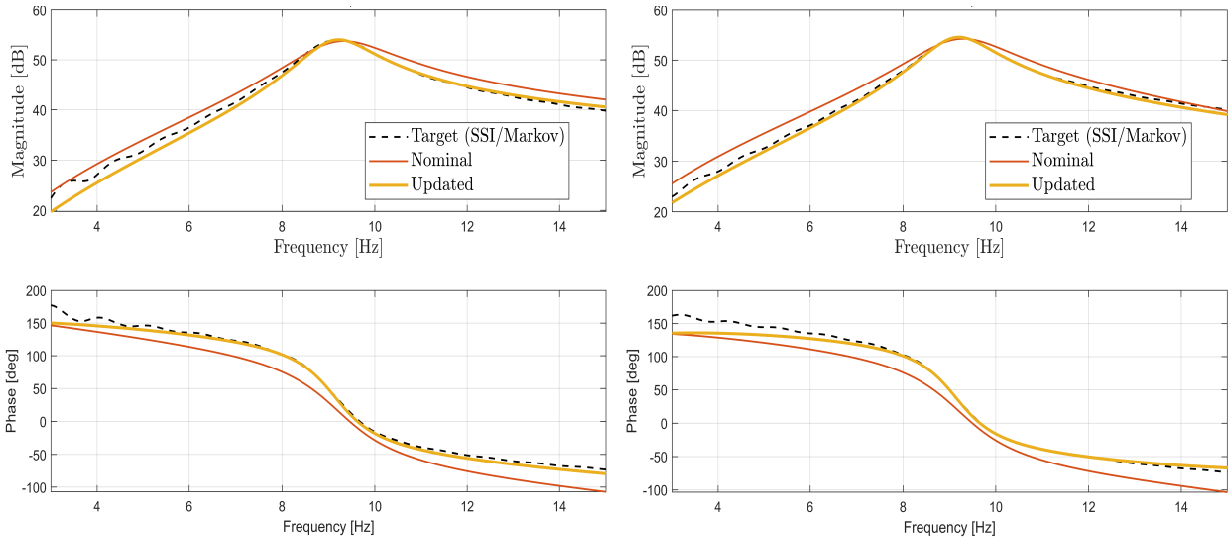
Table 7: Updated control-surface aerodynamic and actuator correction parameters.

Parameter	Input 1	Input 2	Input 3	Input 4
γ_{0x}	-0.25197	-0.39950	-0.20253	0.073287
γ_{1x}	-0.30490	-0.39058	-0.37661	-0.067614
γ_{τ}	0.22068	-0.33240	-0.38670	-0.21286
γ_{K}	-0.33470	-0.29890	-0.35030	-0.39781

5.2 Frequency-domain validation

In addition to the Markov-parameter comparison, the updated model is evaluated in the frequency-domain. The frequency-response functions are used as an independent validation of the input-output behaviour over the relevant frequency range. They are not included as a direct optimization target in the baseline DPSI formulation, but provide an intuitive assessment of the amplitude and phase agreement between the nominal, updated, and identified dynamics. In the following plots Fig.9 and 7, representative frequency-response functions are shown for validation of the updated model.

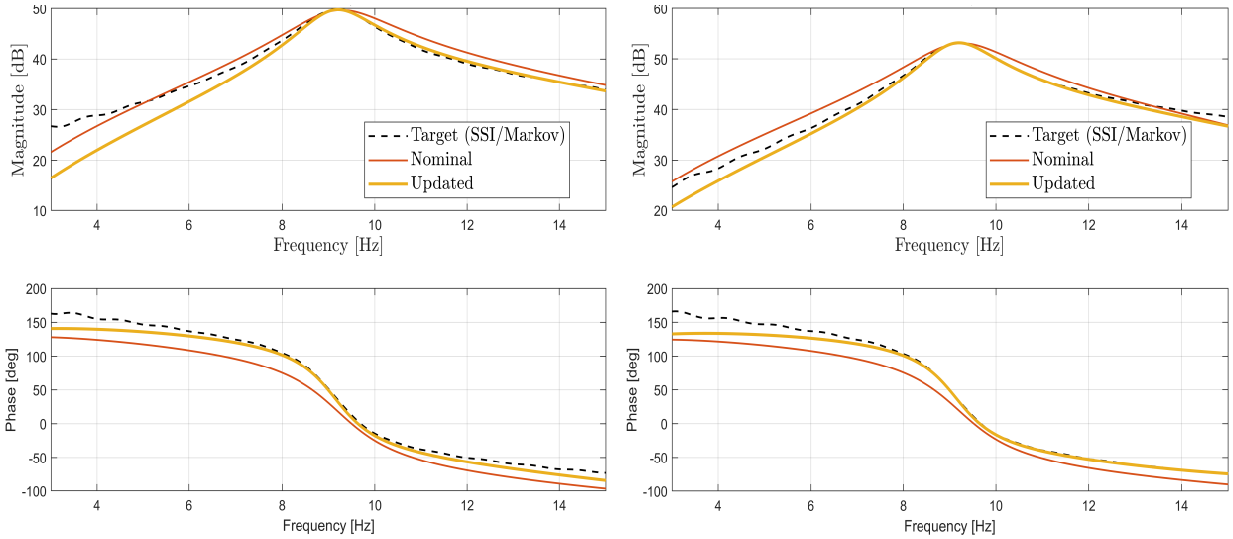
The results show that the DPSI update improves the overall agreement of the model with the experimental dynamics. In the frequency domain, the updated model follows the identified response more closely than the nominal model for the dominant input-output channels.



(a) Frequency-response function $h_{7,4}$ (from flap Nr.4 to sensor 5a)

(b) Frequency-response function $h_{8,4}$ (from flap Nr.4 to sensor 5b)

Figure 6: Frequency-response comparison between the nominal model, updated DPSI model, and identified target model



(a) Frequency-response function $h_{5,4}$ (from flap Nr.4 to sensor 4b)

(b) Frequency-response function $h_{6,4}$ (from flap Nr.4 to sensor 6b)

Figure 7: Frequency-response function comparison between the nominal model, updated DPSI model, and identified target model.

5.3 Time-response validation using Theil's inequality coefficient

The time-response validation is performed using selected experimental validation segments. The same input commands are applied to the nominal and updated models, and the simulated acceleration responses are compared with the measured sensor signals. This comparison assesses whether the improvement obtained in the Markov-parameter domain also leads to improved prediction of measured time histories. Using residual analysis by means of Theil's inequality Coefficient (TIC), we assess the quality of the updated model in time-domain. The TIC provides a normalized measure of the discrepancy between the measured and simulated time responses. For a measured output $y_k^{\text{meas,o}}$ and a simulated response $y_k^{\text{sim,o}}$, it is defined as

$$\text{TIC}_{\text{o}} = \frac{\sqrt{\frac{1}{N}\sum_{k=1}^{N}\left(y_k^{\text{sim,o}} - y_k^{\text{meas,o}}\right)^2}}{\sqrt{\frac{1}{N}\sum_{k=1}^{N}\left(y_k^{\text{sim,o}}\right)^2} + \sqrt{\frac{1}{N}\sum_{k=1}^{N}\left(y_k^{\text{meas,o}}\right)^2}}. \tag{88}$$

The coefficient is bounded between zero and one, where a value close to zero indicates a very good agreement between simulation and measurement. Despite the fact that the acceptable value for TIC_o varies depending on the application, as a general rule, a value < 0.25 indicates an satisfactory agreement [13]. Figure 8 compares the TIC values obtained for the nominal model and the updated model over all acceleration sensor channels. The mean TIC value is reduced from $\text{TIC}_{\text{mean,nom}} = 0.32$ to $\text{TIC}_{\text{mean,upd}} = 0.13$. This corresponds to a relative reduction of approximately $59.4\ \%$. This confirms that the DPSI update improves not only the Markov-parameter agreement with the supplied SSI target model, but also the time-domain response consistency for the selected validation time segments.

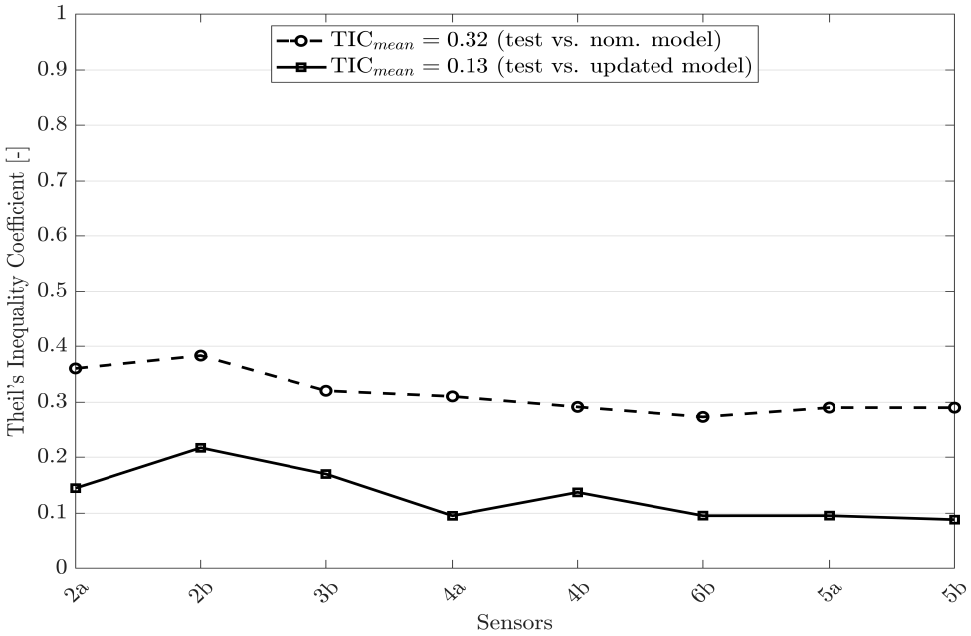
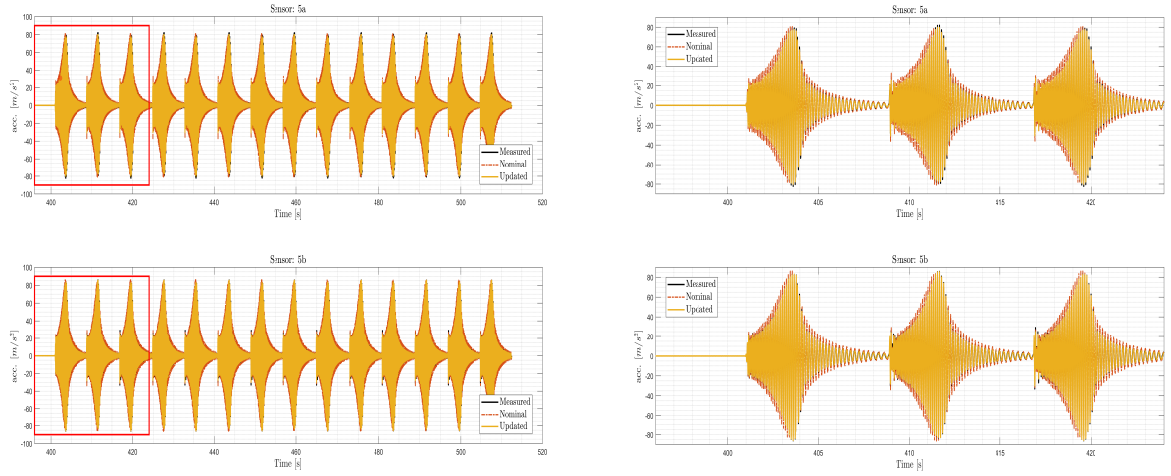


Figure 8: Fit error distribution between wind tunnel test and model (nominal and updated) data for each output

In the following plots in Fig.9, two representative acceleration sensor signals (5a and 5b) located at the wing tip are shown for time-domain validation. The measured responses are compared with the simulated responses of the nominal and updated models using the same input excitation. These signals are selected because the wing-tip sensors are particularly sensitive to the dominant flexible deformation of the wing and therefore provide a useful assessment of the dynamic response improvement after the DPSI update.



(a) Measured and simulated accelerations at the sensor 5a and 5b

(b) Measured and simulated accelerations at the sensor 5a and 5b (zoomed view)

Figure 9: Time-response comparison of the measured wing-tip acceleration signals with the nominal and updated model responses. The enlarged view highlights the local response agreement and shows the improved tracking of the measured dynamics after the DPSI update.

In the time domain, the updated response shows improved correlation with the measured accelerations, which is also reflected in the reduced Theil's Inequality Coefficient.

6 CONCLUSION

This work presented a directly-physical subspace identification approach for structure-preserving aeroservoelastic model updating. The main novelty of the method is the combination of data-driven subspace identification targets with a physically parameterized continuous-time aeroservoelastic model. Instead of replacing the nominal model by a black-box identified realization, the proposed DPSI formulation updates physically meaningful parameters while preserving the state-space structure associated with structural dynamics, unsteady aerodynamics, actuator dynamics, aerodynamic lag states, and sensor-output dynamics.

A central advantage of the method is the use of Markov parameters as realization-independent input-output targets. This avoids a direct comparison between the arbitrary state coordinates of the subspace-identified model and the physical coordinates of the aeroservoelastic model. The updated model is assembled directly in continuous time for every candidate parameter vector and is only discretized for comparison with the identified Markov sequence. Therefore, no discrete-to-continuous back transformation of a black-box model is required.

The wind-tunnel application demonstrated that the proposed update strategy can significantly improve the input-output behaviour of the nominal model while maintaining physical interpretability. The Markov-parameter mismatch was reduced by approximately $49.59\ \%$, and the time-response validation showed a reduction of the mean Theil's Inequality Coefficient from 0.32 to 0.13. These results indicate that the updated model provides a more accurate representation of the measured dynamics while retaining a physically meaningful model structure.

The optimized parameters show that the observed improvement is achieved through a combined correction of structural, aerodynamic, and actuator-related quantities. This illustrates the benefit of a directly physical parameterization: the update does not merely improve numerical input-output agreement, but also provides insight into which physical model components contribute to the discrepancy between the nominal and identified dynamics.

Overall, the proposed DPSI framework provides a useful intermediate approach between purely black-box system identification and conventional physics-based model updating. It exploits the accuracy of subspace identification while preserving the interpretability and usability of a structured aeroservoelastic model. Future work should focus on refined sensor-chain and delay modelling, improved calibration, and optional mode-tracking-based constraints when accurate modal-parameter agreement is required.

7 REFERENCES

[1] Van Overschee, P. and De Moor, B. (1996). *Subspace Identification for Linear Systems: Theory, Implementation, Applications*. Kluwer Academic Publishers.

[2] Ljung, L. (1999). *System Identification: Theory for the User*. Prentice Hall, 2 ed.

[3] Katayama, T. (2005). *Subspace Methods for System Identification*. Springer.

[4] Albano, E. and Rodden, W. P. (1969). A doublet-lattice method for calculating lift distributions on oscillating surfaces in subsonic flows. *AIAA Journal*, 7(2), 279–285. doi: 10.2514/3.5086.

[5] Rodden, W. P., Taylor, P. F., and McIntosh, S. C. (1998). Further refinement of the subsonic doublet-lattice method. *Journal of Aircraft*, 35(5), 720–727. doi:10.2514/2.2382.

[6] Roger, K. L. (1977). Airplane math modeling methods for active control design. In *AGARD Conference Proceedings No. 228, Structural Aspects of Active Controls*. pp. 4–1–4–11.

[7] Karpel, M. (1982). Design for active flutter suppression and gust alleviation using state-space aeroelastic modeling. *Journal of Aircraft*, 19(3), 221–227.

[8] Doggett, R. V. (1973). A one-dimensional spline technique for the transfer of aerodynamic forces on an elastic wing. Nasa technical report, NASA.

[9] Harder, R. L. and Desmarais, R. N. (1972). Interpolation using surface splines. *Journal of Aircraft*, 9(2), 189–191.

[10] Ho, B. L. and Kalman, R. E. (1966). Effective construction of linear state-variable models from input/output functions. *Regelungstechnik*, 14, 545–548.

[11] Juang, J.-N. and Pappa, R. S. (1985). An eigensystem realization algorithm for modal parameter identification and model reduction. *Journal of Guidance, Control, and Dynamics*, 8(5), 620–627.

[12] Schmidt, T. G., Volkmar, R., Micheli, B., et al. (2025). Assessing sensor-model-fusion technologies on a flexible aeroelastic wing demonstrator through wind tunnel testing in the dlr project safer2. In *Deutscher Luft- und Raumfahrtkongress 2025*. Augsburg, Germany. DLRK 2025, 23–25 September 2025.

[13] Özge Süelözgen. *Application and Validation of a Model Updating Approach for Linearized State-Space Models of Flexible Aircrafts Using Multiple Flight Test Data*. doi: 10.2514/6.2023-0374.

COPYRIGHT STATEMENT

The authors confirm that they, and/or their company or organisation, hold copyright on all of the original material included in this paper. The authors also confirm that they have obtained permission from the copyright holder of any third-party material included in this paper to publish it as part of their paper. The authors confirm that they give permission, or have obtained permission from the copyright holder of this paper, for the publication and public distribution of this paper as part of the IFASD 2026 proceedings or as individual off-prints from the proceedings.